We are IntechOpen,
the world's leading publisher of
Open Access books
Built by scientists, for scientists

4,800
Open access books available

122,000
International authors and editors

135M
Downloads

Our authors are among the

154
Countries delivered to

TOP 1%
most cited scientists

12.2%
Contributors from top 500 universities

BOOK CITATION INDEX INDEXED

WEB OF SCIENCE™

Selection of our books indexed in the Book Citation Index
in Web of Science™ Core Collection (BKCI)

Interested in publishing with us?
Contact book.department@intechopen.com

Numbers displayed above are based on latest data collected.
For more information visit www.intechopen.com

GNSS Atmospheric and Ionospheric Sounding – Methods and Results

Shuanggen Jin
Shanghai Astronomical Observatory, Chinese Academy of Sciences
China

1. Introduction

The GPS atmospheric and ionospheric delays have been considered as an error source for a long time. In 1992 when the GPS became fully operational, Ware (1992) suggested limb sounding the Earth atmosphere using GPS atmospheric delay signals. In April 1995, the small research satellite of Microlab-1 was successfully put into a Low Earth Orbit (LEO) to validate the GPS radio occultation method (Feng and Herman, 1999). Since then, the GPS/Meteorology Mission (GPS/MET) has been widely used to produce accurate, all weather pressure, temperature, density profiles in the troposphere and the ionospheric total electron content (TEC) as well as electron density profiles (Rocken, 1997; Hajj and Romans, 1998; Syndergaard, 2000), to improve weather analysis and forecasting, monitor climate change, and monitor ionospheric events. While traditional observing instruments, e.g. water vapour radiometer (WVR), incoherent scatter radars (ISR), ionosonde, topside sounders onboard satellites, in situ rocket and satellite observations, are expensive and also partly restricted to either the bottomside ionosphere or the lower part of the topside ionosphere (usually lower than 800 km), such as ground based radar ionospheric measurements. While GPS satellites in high altitude orbits (~20,200 km) are capable of providing details on the structure of the entire atmosphere, even the plasma-sphere. Moreover, GPS is a low-cost, all-weather, near real time, and high-temporal resolution (1~30s) technique. Therefore, GPS is a powerful tool to sound the atmosphere and ionosphere as well as their application in meteorology, climate and space weather.

2. Tropospheric sounding

The tropospheric delay of GPS signal through the neutral atmosphere was one of major error sources in navigation and positioning, which contributes a bias in height of several centimetres (Tregoning et al. 1998). Nowadays, GPS has been used to determine the zenith tropospheric delay (ZTD) (Jin and Park, 2005) through mapping functions (Niell, 1996). The ZTD is the integrated refractivity along a vertical path through the neutral atmosphere:

$$ZTD = c\tau = 10^{-6} \int_0^\infty N(s)ds \qquad (1)$$

where c is the speed of light in a vacuum, τ is the delay measured in units of time and N is the neutral atmospheric refractivity. The N is empirically related to standard meteorological variables as (Davis et al. 1985)

$$N = k_1\rho + k_2\frac{P_w}{Z_wT} + k_3\frac{P_w}{Z_wT^2}$$ (2)

where $k_i(i=1,2,3)$ is constant, ρ is the total mass density of the atmosphere, P_w is the partial pressure of water vapor, Z_w is a compressibility factor near unity accounting for the small departures of moist air from an ideal gas, and T is the temperature in degrees Kelvin. The integral of the first term of equation (2) is the hydrostatic component (N_h) and the integral of the remaining two terms is the wet component (N_w). Thus, ZTD is the sum of the hydrostatic or dry delay (ZHD) and non-hydrostatic or wet delay (ZWD), respectively. The dry component ZHD is related to the atmospheric pressure at the surface, while the wet component ZWD can be transformed into the precipitable water vapor (PWV) and plays an important role in energy transfer and in the formation of clouds via latent heat, thereby directly or indirectly influencing numerical weather prediction (NWP) model variables (Bevis et al, 1994; Tregoning et al. 1998; Manuel et al., 2001). Therefore, the Zenith Tropospheric Delay (ZTD) is an important parameter of the atmosphere, which reflects the weather and climate processes, variations, and atmospheric vertical motions, etc.

In the last decade, ground-based GPS receivers have been developed as all-weather, high spatial-temporal resolution and low-cost remote sensing systems of the atmosphere (Bevis et al., 1994; Manuel et al., 2001), as compared to conventional techniques such as satellite radiometer sounding, ground-based microwave radiometer, and radiosondes (Westwater, 1993). With independent data from other instruments, in particular water vapor radiometers, it has been demonstrated that the total zenith tropospheric delay or integrated water vapor can be retrieved using ground based GPS observations at the same level of accuracy as radiosondes and microwave radiometers (Elgered et al. 1997; Tregoning et al. 1998). Currently, the International GPS Service (IGS) has operated a global dual frequency GPS receiver observation network with more than 350 permanent GPS sites since 1994 (Beutler et al., 1999). It provides a high and wide range of scales in space and time to study seasonal and secular variations of ZTD as well as its possible climate processes.

2.1 GPS data and analysis

The IGS (International GPS Service) was formally established in 1993 by the International Association of Geodesy (IAG), and began routine operations on January 1, 1994 (Beutler et al. 1999). The IGS has developed a worldwide network of permanent tracking stations with more than 350 GPS sites, and each equipped with a GPS receiver, providing raw GPS orbit and tracking data as a data format called Receiver Independent Exchange (RINEX). All available near-real-time global IGS observation data archived in the Global IGS Data Center, which contributes to geodesy and atmosphere research activities in a global scale. Here the globally distributed 150 IGS sites with better continuous observations are selected with spanning at least four years of measurements (Figure 1), and most sites observations are from 1994 to 2006.
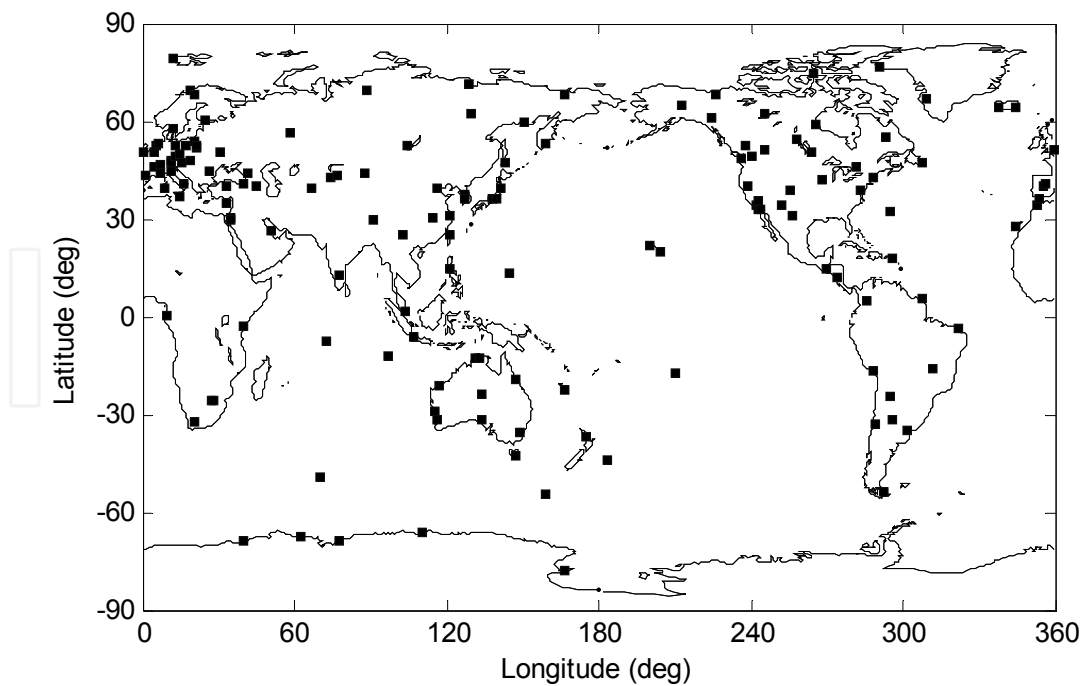
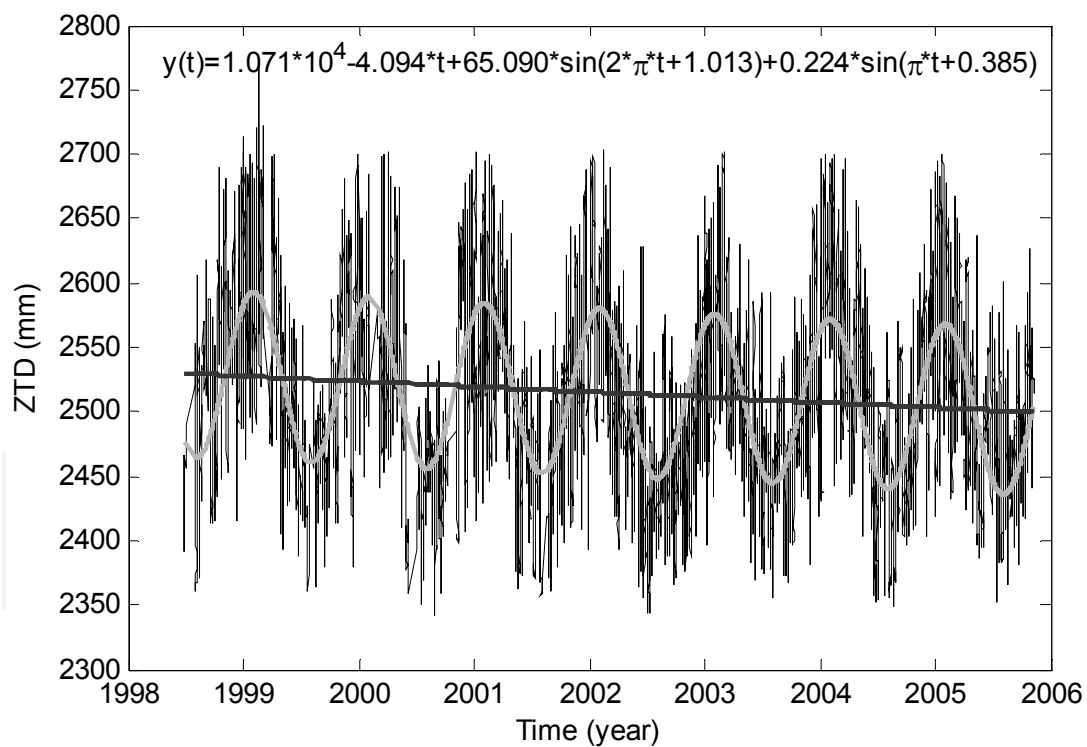Fig. 1. The distribution of global IGS GPS sites

Fig. 2. ZTD time series at TOW2 station, Australia. The solid line is the fitting results, consisting of a linear decrease and seasonal components

2.2 Zenith tropospheric delay retrieval

The processing software must resolve or model the orbital parameters of the satellites, solve for the transmitter and receiver positions, account for ionospheric delays, solve for phase

cycle ambiguities and the clock drifts in addition to solving for the tropospheric delay parameters of interest. We use the GAMIT software (King and Bock 1999), which solves for the ZTD and other parameters using a constrained batch least squares inversion procedure. In addition, this study uses the newly recommended strategies (Byun et al. 2005) to calculate ZTD time series with temporal resolution of 2 hours from 1994 to 2006. The GAMIT software parameterizes ZTD as a stochastic variation from the Saastamoinen model (Saastamoinen 1972), with piecewise linear interpolation in between solution epochs. GAMIT is very flexible in that it allows a priori constraints of varying degrees of uncertainty. The variation from the hydrostatic delay is constrained to be a Gauss-Markov process with a specified power density of $2\,\mathrm{cm}/\sqrt{hour}$, referred to below as the "zenith tropospheric parameter constraint". We designed a 12-hour sliding window strategy in order to process the shortest data segment possible without degrading the accuracy of ZTD estimates. The ZTD estimates are extracted from the middle 4 hours of the window and then move the window forward by 4 hours. Finally, the ZTD time series from 1994 to 2006 are obtained at globally distributed 150 IGS sites with temporal resolution of 2 hours. For example, Figure 2 shows the times series of zenith total delay (ZTD) (upper) at TOW2 station, Australia.

2.3 Global mean zenith tropospheric delay

The ZTD consists of the hydrostatic delay (ZHD) and wet delay (ZWD). The ZHD can be well calculated from surface meteorological data, ranging 1.5-2.6 meters, which accounts for 90% of ZTD. It derives from the relationship with hydrostatic equilibrium approximation for the atmosphere. Under hydrostatic equilibrium, the change in pressure with height is related to total density at the height h above the mean sea level by

$$dp = -\rho(h)g(h)dh \qquad (3)$$

where $\rho(h)$ and g(h) are the density and gravity at the height h. It can be further deduced as

$$ZHD = kp0 \qquad (4)$$

where k is constant (2.28 mm/hPa) and p_0 is the pressure at height h_0 (Davis et al. 1985). It shows that the ZHD is proportional to the atmospheric pressure at the site. The ZWD is highly variable due possibly to varying climate, relating to the temperature and water vapour. The mean ZTD values at all GPS sites are shown in Figure 3 as a color map. It has noted that lower ZTD values are found at the areas of Tibet (Asia), Andes Mountain (South America), Northeast Pacific and higher latitudes (Antarctica and Arctic), and the higher ZTD values are concentrated at the areas of middle-low latitudes. In addition, the ZTD values decrease with increasing altitude, which is due to the atmospheric pressure variations with the height increase. Atmospheric pressure is the pressure above any area in the Earth's atmosphere caused by the weight of air. Air masses are affected by the general atmospheric pressure within the mass, creating areas of high pressure (anti-cyclones) and low pressure (depressions). Low pressure areas have less atmospheric mass above their locations, whereas high pressure areas have more atmospheric mass above their locations. As elevation increases, there are exponentially, fewer and fewer air molecules. Therefore, atmospheric pressure decreases with increasing altitude at a decreasing rate. The following relationship is a first-order approximation to the height (http://www.chemistrydaily.com/ chemistry/Atmospheric_pressure):

$$\log_{10} P \approx 5 - \frac{h}{15.5} \qquad (5)$$

where P is the pressure in Pascals and h is the height in millimeters. Based on the Eq. (4), ZHD can be expressed as $2.28*10^{(5-h/15.5)}$. Therefore, ZTD at all GPS sites can be approximately expressed as:

$$ZTD = 2.28*10^{(5-h/15.5)} \qquad (6)$$

where the units of ZTD and h are in millimeters, respectively. Comparing GPS-derived ZTD with the empirical formula estimations, it has shown a good consistency.
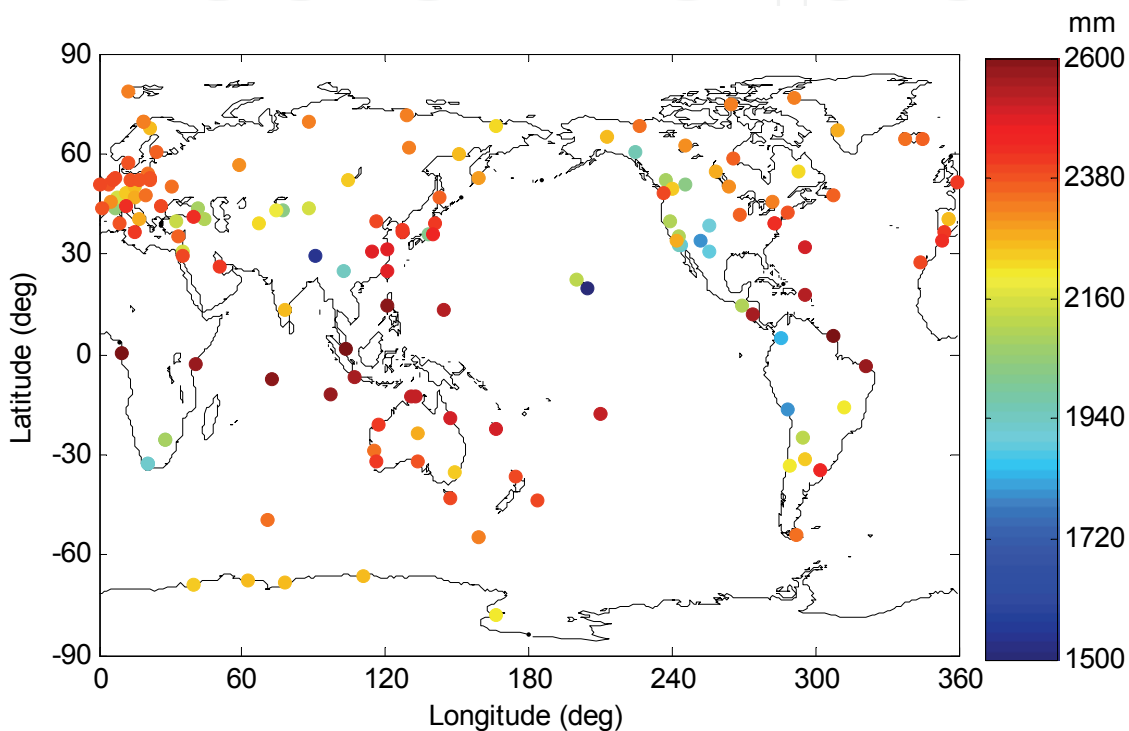

Fig. 3. Distribution of mean ZTD at global IGS sites

2.4 Trend analysis

The GPS ZTD time series have been analyzed for 4-12 years at globally distributed 150 GPS sites. Using the least square the fitting parameters of all GPS site are obtained, including trend and seasonal variation terms (Jin et al., 2007). The mean secular ZTD variation trend is about 1.5±0.001 mm/yr. Figure 4 shows the distribution of the secular ZTD variation trends at all GPS sites as the yearly increase or decrease. It can be seen that the trends are positive in most parts of the Northern Hemisphere and negative in most parts of the Southern Hemisphere (excluding positive in Antarctic), corresponding to a systematic increase or decrease of ZTD. It is interesting to note that the downtrend in Australia is larger than other regions. This downtrend of ZTD is probably due to the highly deserted in Australia. In addition, the ZTD variation trend decreases with increasing altitude, and furthermore, the ZTD trends are almost symmetrical with altitude. This indicates that the secular ZTD variations are larger at the lower altitude and at the higher altitude the secular ZTD variations hardly increase or decrease. In addition, the sum of downward and upward

trends at globally distributed GPS sites is almost zero, which possibly indicates that the secular variation is in balance at a global scale, but subjecting to unevenly distributed GPS stations, etc. It need further be confirmed with much denser GPS network in the future. These secular ZTD variation characteristics reflect the total variations of surface atmospheric pressure, temperature and relative humidity, atmospheric vertical motions, etc.
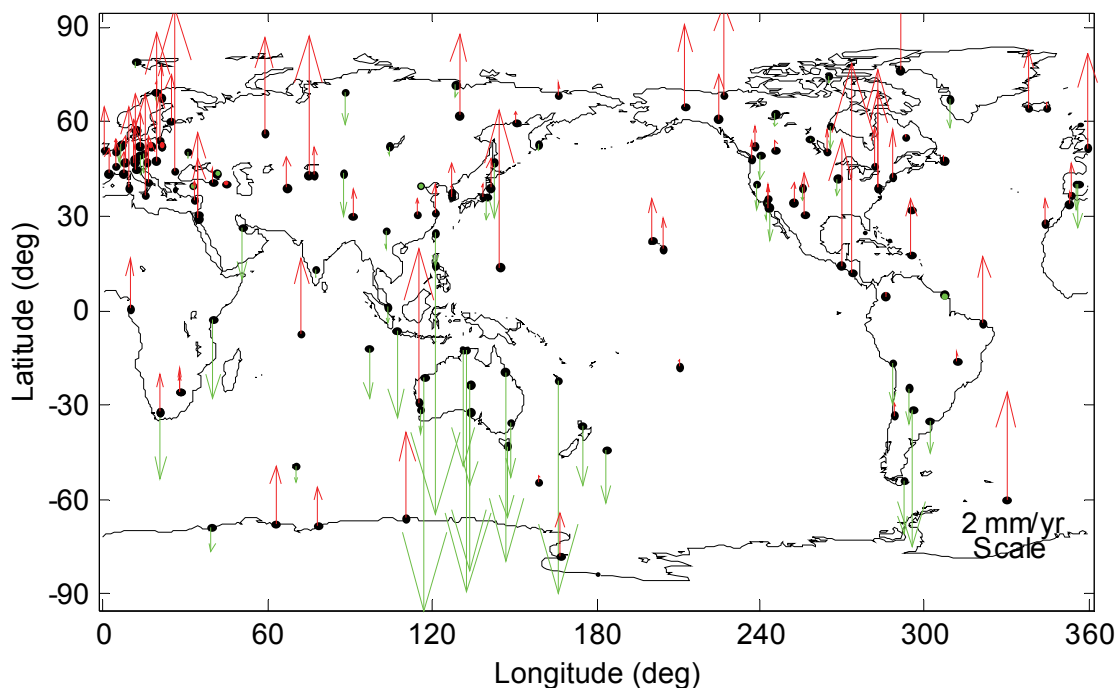

Fig. 4. Secular trend of ZTD variations at global IGS sites. The red upwards arrows represent the increase of secular ZTD variations and the green downwards arrows stand for the decrease of secular ZTD variations

2.5 Seasonal cycles

Meanwhile, the seasonal components are also obtained using least square at annual and semi-annual scales, which can be used to study the seasonal cycle, including amplitude and phase shift. The fitted phase shift is used to determine in which month the seasonal maximum takes place. The annual variation of ZTD ranges from 25 to 75 mm depending on the site, and the average amplitude is about 50 mm at most sites (Fig. 5). The annual variation amplitudes of ZTD at the IGS sites near Oceanic coasts are generally larger than in the continental inland. In addition, larger amplitudes of annual ZTD variation are mostly found at middle-low latitudes (near 20S° and 40N°), and the amplitudes of annual ZTD variation are especially smaller at higher latitudes (e.g. Antarctic and Arctic) and the equator areas (see Fig. 6). Sites on the eastern Atlantic and northeast Pacific coasts have lower annual variations, probably because of the moderating effect of the ocean on climate. Sites on the lee side of the Alps have higher annual variation, possibly due to the combined effects of a rain shadow in the winter and high moisture from the Mediterranean in the summer (Haase et al., 2003; Deblonde et al., 2005). Figure 7 shows the annual phase distribution with the latitude, where phase values are counted as clockwise from the north. It can be seen that the phase of annual ZTD variation is almost found at about 60° (about February, summer) in the Southern Hemisphere and at about 240° (about August, summer) in the Northern Hemisphere, which is just a half-year difference.
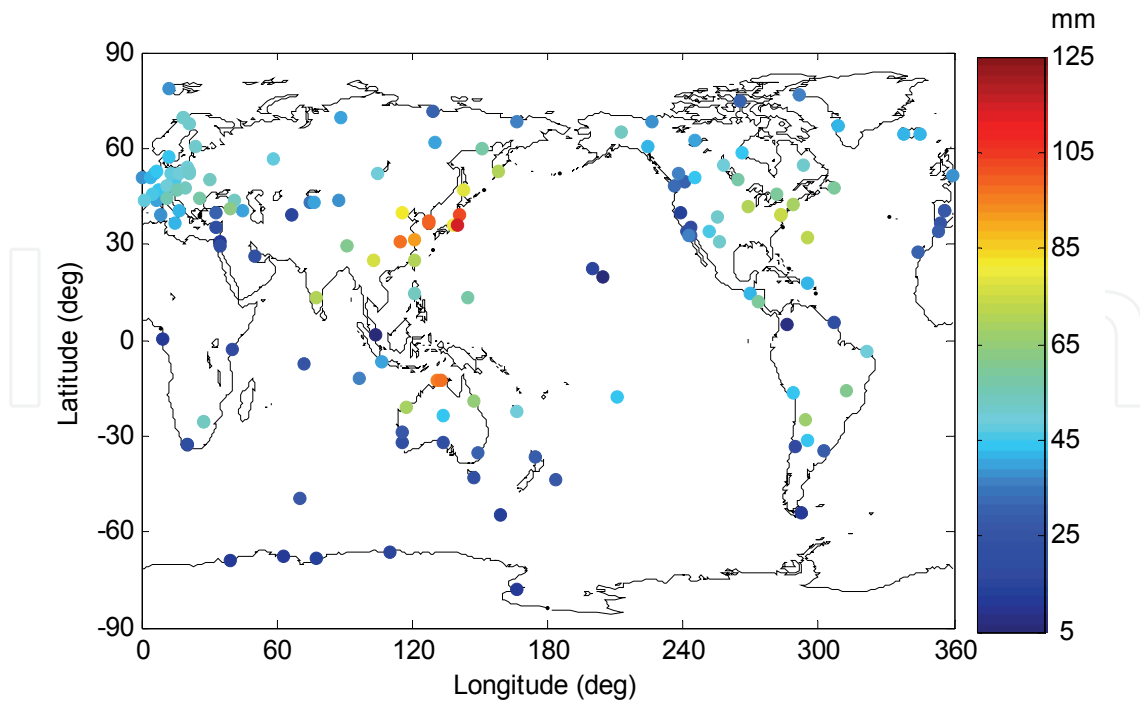
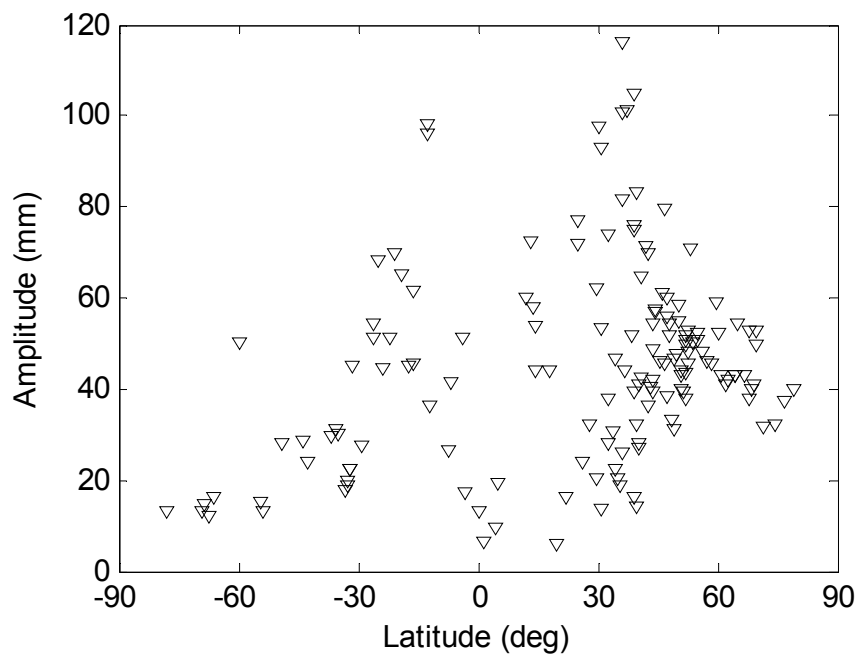Fig. 5. Annual variation amplitude of ZTD at globally distributed 150 GPS sites

Fig. 6. Distribution of annual ZTD variation amplitude with the latitude

The mean amplitude of semiannual ZTD variations is much smaller than annual variations with about 10 mm. The amplitudes of the semiannual oscillations are much smaller on the Southern Hemisphere than on the Northern Hemisphere. The distribution of the semiannual variation phase with the latitude has no clear symmetry. For example, at the latitudes of 40°N-50°N in the Northern Hemisphere, the semiannual phase is about 30° (about January), while at the latitudes of 40°S-50°S in the Southern Hemisphere, the semiannual phase is about 330° (November).

Although the ZWD is small accounting for about 10 percent of the total zenith tropospheric delay (ZTD), the seasonal cycle in ZTD is due primarily to the wet component (ZWD). Furthermore, the seasonal variation phases of ZTD are almost consistent with surface temperature variations with the correlation coefficient of about 0.8. This reflects that annual and semiannual variations of ZTD are due mainly to the ZWD variations, about 80% in the surface temperature and 20% mainly in water vapour variations.
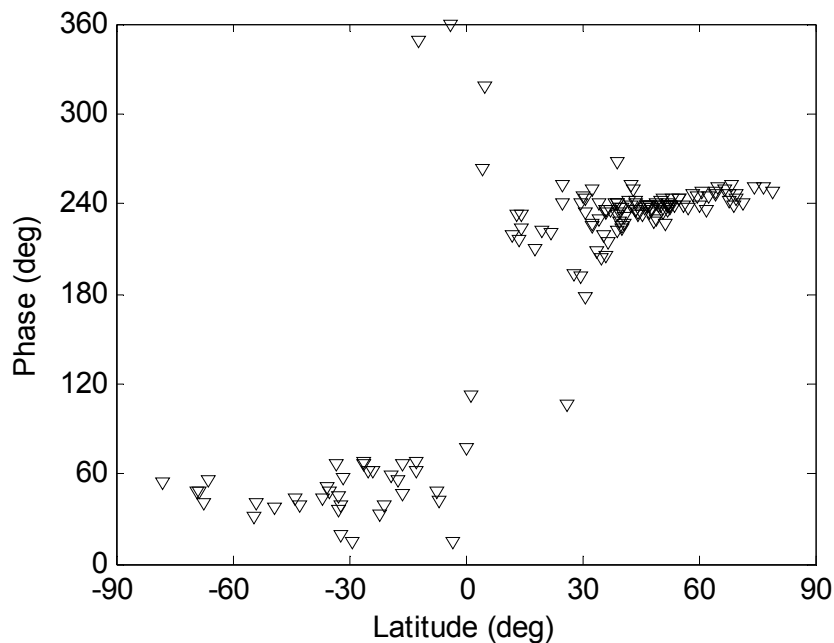

Fig. 7. Distribution of annual variation phase with the latitude. The phases are counted as clockwise from the north

2.6 Diurnal and semidiurnal ZTD cycles

The 4-7 years of GPS-derived ZTD time series has been used to analyze the diurnal and semidiurnal ZTD cycles and their features. Fig. 8a shows a colour coded map of diurnal ZTD amplitudes derived from the GPS data. The diurnal cycle (S1) has amplitudes between 0.2 and 10.9 mm with an uncertainty of about 0.5 mm. The diurnal ZTD amplitudes reduce with increasing latitude with the largest amplitudes appearing in the low-latitude equatorial areas, in particular in tropical Asia and the Gulf of Mexico. At these low latitudes, amplitudes of up to 10.9 mm are observed, while the high latitude areas reveal generally lower diurnal ZTD amplitudes. The peak values of the diurnal cycles occur spreading over the whole day (Fig. 9a). For the European stations there appears to be a preference for the second half of the day. At the semidiurnal cycle (S2), amplitudes between 0.1 and 4.3 mm with an uncertainty of about 0.2 mm are observed. Similar to the diurnal results mentioned above, the largest semidiurnal amplitudes are also found in low-latitude equatorial areas. The first peak of the semidiurnal cycle occurs typically around local noon. These diurnal and semidiurnal cycles of ZTD may be due to certain short time scale physical processes such as diurnal convection, atmospheric tides, general circulation and the coupling between the lower and the middle and upper atmosphere.

From Eq. (4), the zenith hydrostatic delay (ZHD) can be written as ZHD=2.28 p0. The scale factor k varies less than 1% even under severe weather conditions. As the hydrostatic
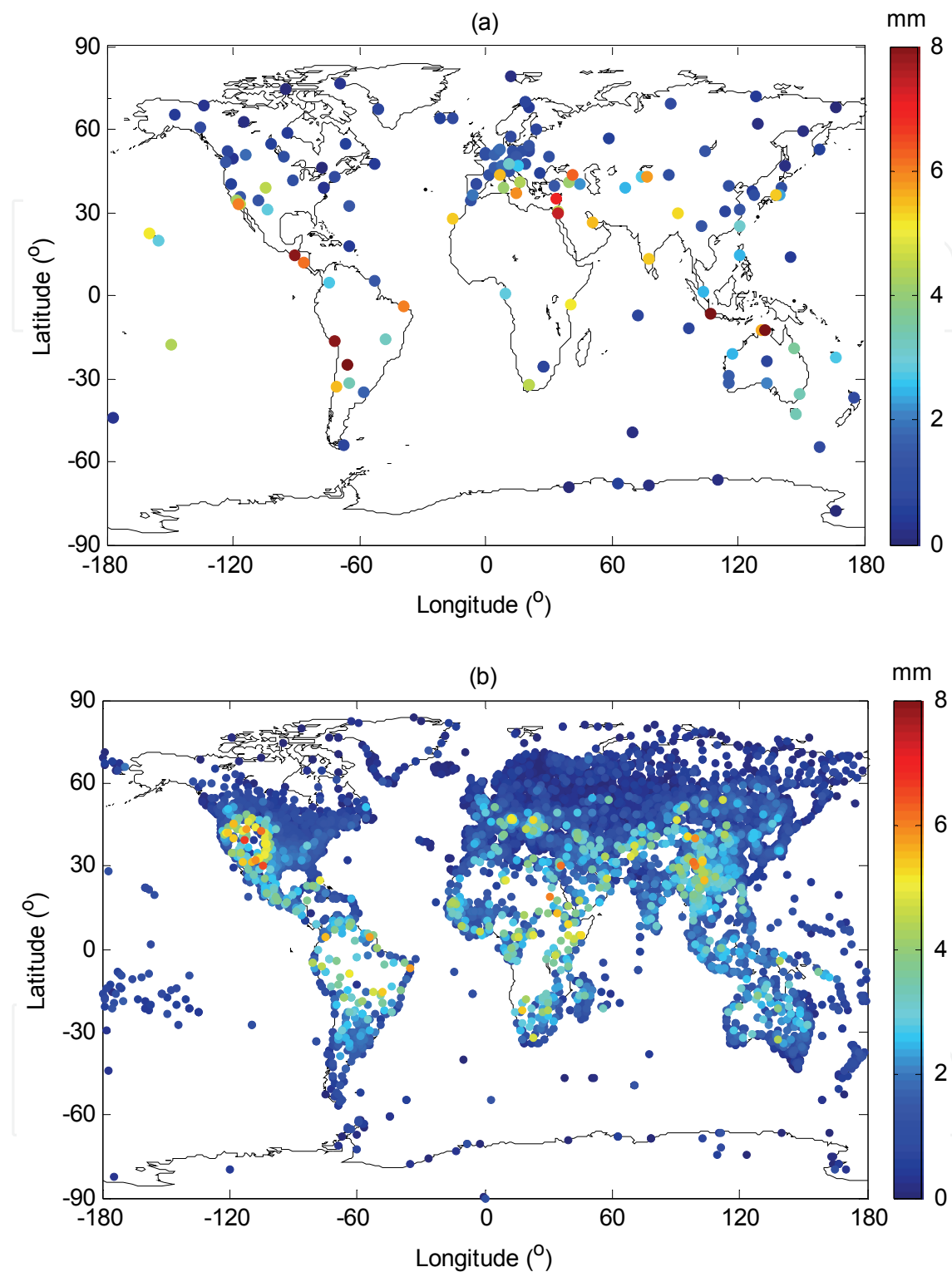
Fig. 8. Diurnal variation amplitudes (mm). (a) from GPS-derived ZTD and (b) from COADS surface pressure data adjusted by a scale factor (2.28 mm/hPa)

component ZHD accounts for approximately 90% of ZTD, ZTD is strongly correlated with surface pressure p_0 at the site. It can be seen that if subdiurnal surface pressure varies by 1 hPa, the scale factor predicts a subdiurnal ZTD variation with amplitude of 2.28 mm. The
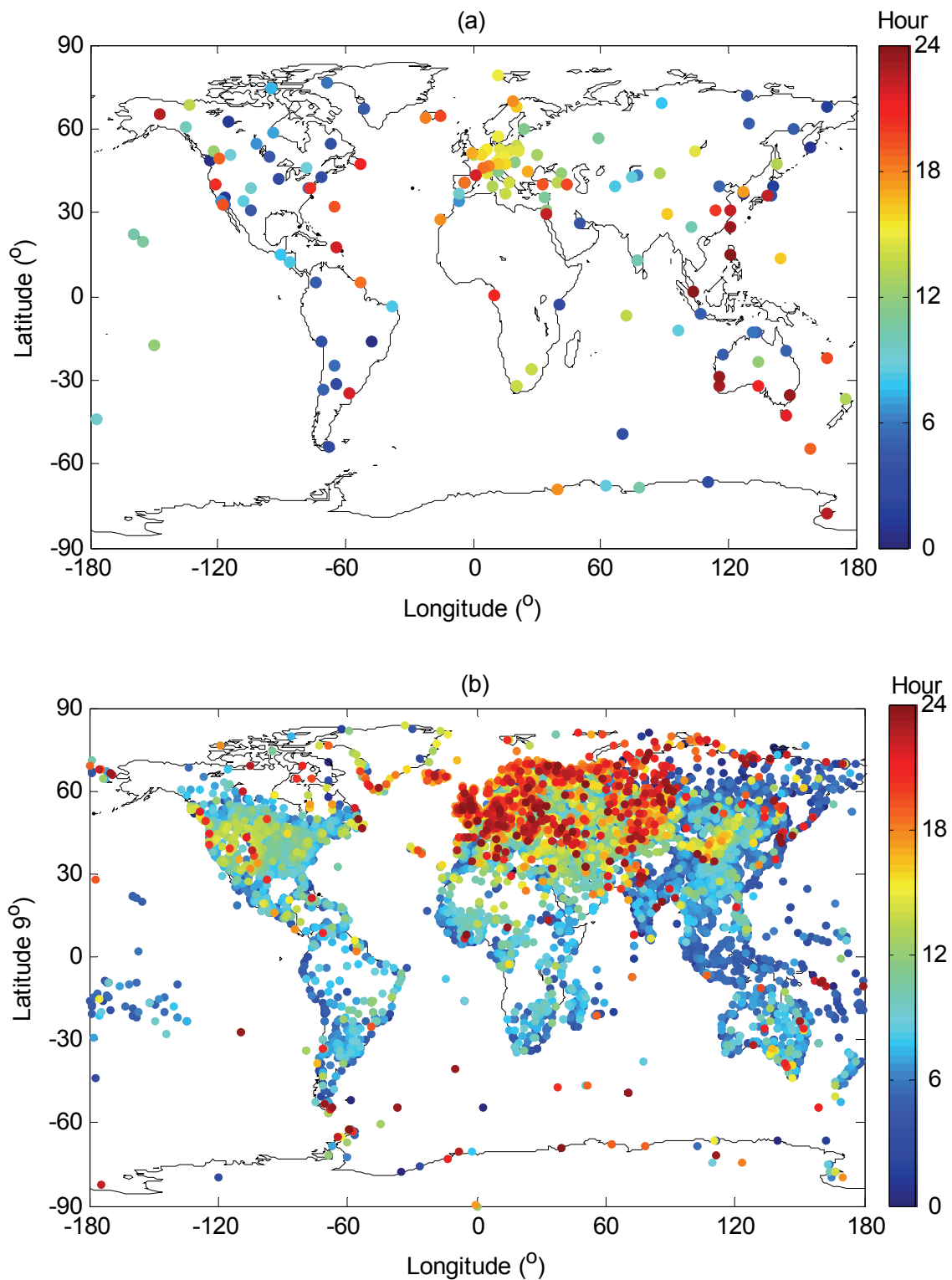
Fig. 9. Time of diurnal peak values at local time (LT: hour) where at each GPS sites longitude the Sun is at its highest elevation at 12:00 LT. (a) from global IGS GPS observations and (b) from COADS surface pressure data

GPS-derived S1 and S2 signals in ZTD are compared with three-hour surface synoptic pressure observations from 1997 to 2007 that are archived at the National Center for

Atmospheric Research (NCAR) (DS464.0; (http://dss.ucar.edu/datasets/ds464.0). Notably, these results are adjusted by a scale factor 2.28 mm/hPa, which are accounted for in the comparison. These pressure data origin from more than 8000 land and ocean weather stations including the Global Telecomuncation System (GTS) and marine reports from the Comprehensive Ocean-Atmosphere Data Set (COADS) (Dai and Wang 1999). The plots of diurnal and semidiurnal ZTD cycles show general similarities, indicating that the diurnal and semidiurnal atmospheric tides are probably the main driver of the diurnal and semidiurnal ZTD variations derived from GPS (Jin et al., 2009).

3. Ionospheric sounding

The GPS consists of a constellation of 24 operating satellites in six circular orbits 20,200 km above the Earth at an inclination angle of 55° with a 12-h period. The satellite transmits two frequencies of signals (f1 = 1575.42 MHz and f2 = 1227.60 MHz). The equations of carrier phase (L) and code observations (pseudorange P) of double frequency GPS can be expressed as follows:

$$L_{k,j}^i = \lambda_k \phi_{k,j}^i = \rho - d_{ion,k,j}^i + d_{trop,j}^i + c(\tau^i - \tau_j) - \lambda_k(b_{k,j}^i + N_{k,j}^i) \tag{7}$$

$$P_{k,j}^i = \rho + d_{ion,k,j}^i + d_{trop,j}^i + c(\tau^i - \tau_j) + d_{q,k}^i + d_{q,k,j} + \varepsilon_j^i \tag{8}$$

where superscript i and subscript j represent the satellite and ground-based GPS receiver, respectively, ρ is the distance between satellite i and GPS receiver j, d_{ion} and d_{trop} are the ionospheric and tropospheric delays, respectively, c is the speed of light in vacuum space, τ is the satellite or receiver clock offset, b is the phase delay of satellite and receiver instrument bias, d_q is the code delay of satellite and receiver instrumental bias, λ is the carrier wavelength, ϕ is the total carrier phase between the satellite and receiver, N is the ambiguity of carrier phase, and ε is the other residuals. From Eq.(7) and (8), the ionospheric delay can be determined, which is useful for ionospheric delay correction and space weather.

3.1 2-D ionospheric imaging

The ionospheric delay can be determined from the double frequency GPS phase and code (pseudorange) observations as

$$L_4 = \phi_{1j}^i - \phi_{2j}^i = -40.3\left(\frac{1}{f_1^2} - \frac{1}{f_2^2}\right)F(z)VTEC(\beta,s) + B_4 \tag{9}$$

$$P_4 = P_{1j}^i - P_{2j}^i = 40.3\left(\frac{1}{f_1^2} - \frac{1}{f_2^2}\right)F(z)VTEC(\beta,s) + b_4 \tag{10}$$

where $F(z)$ is the mapping function, B_4 is $\left(B_4 = -\lambda_1(b_{1j}^i + N_{1j}^i) + \lambda_2(b_{2j}^i + N_{2j}^i)\right)$, and b_4 is $(dq_{1j} - dq_{2j}) + (dq_1^i - dq_2^i)$. The Differential Code Biases (b_4) can be obtained through GPS carrier phase observations, and B_4 can be obtained through the formula, $\sum_{i=1}^{N}(p_4 + L_4 - b_4)/N$, where N is the epoch of GPS observation (Jin et al., 2008). For the TEC representation, a

single layer model (SLM) ionosphere approximation was used. SLM assumes that all the free electrons are contained in a shell of infinitesimal thickness at altitude H (generally 350 km above the Earth). A mapping function is used to convert the slant TEC into the vertical TEC (VTEC) as shown:

$$F(z) = \sqrt{(1 - R\cos(90 - z)/(R + H))} \qquad (11)$$

where R is Earth radius, H is SLM height, and z is satellite zenith angle. When using the above mapping function, F(z), one can obtain VTEC values at the ionosphere pierce points (IPPs). The GPS-derived TEC can correct ionospheric delay for microwave techniques and monitor space weather events.

3.2 3-D ionospheric tomography reconstruction

The STEC is defined as the line integral of the electron density as expressed by:

$$STEC = \int_{R_{receiver}}^{R_{satellite}} N_e(\lambda, \varphi, h) ds \qquad (12)$$

where $N_e(\lambda, \varphi, h)$ is the ionospheric electron density, λ, φ and h are the longitude, latitude and height, respectively. To obtain N_e, the ionosphere is divided into grid pixels with a small cell where the electron density is assumed to be constant, so that the STEC in Eq.(4) along the ray path i can be approximately written as a finite sum over the pixels j as follows:

$$STEC_i = \sum_{j=1}^{M} a_{ij} n_j \qquad (13)$$

where a_{ij} is a matrix whose elements denote the length of the path-pixel intersections in the pixel j along the ray path i, and n_j is the electron density for the pixel j. Each set of STEC measurements along the ray paths from all observable satellites at consecutive epochs are combined with the ray path geometry into a linear expression:

$$Y = Ax + \varepsilon \qquad (14)$$

where Y is a column of m measurements of STEC, x is a column of n electron density unknowns for cells in the targeted ionosphere region, and A is an m × n normal matrix with elements a_{ij}. The unknown electron densities x can be estimated by the ionospheric tomographic reconstruction technique. Many tomography algorithms are used in different ways, e.g. algebraic reconstruction technique (Gordon et al., 1970). One of the most common approaches is the algebraic reconstruction technique (ART), which was first introduced in Computerized Ionospheric Tomography (CIT) by Austen et al. (1986). This is an iterative procedure for solving a linear equation. A modified version of ART is the so-called multiplicative ART (MART), where the correction in each iteration is obtained by making a multiplicative modification to x (Raymund et al., 1990; Tsai et al., 2002). The ART generally produces estimates of the unknown parameters by minimization of the L2 norm, while the MART follows maximum entropy criteria and thus underlies different statistics. In addition,

the MART performs a multiplicative modification in each iteration, and thus the inversion results are always positive. Therefore, MART has the advantage over ART in determining the electron densities that avoid unreasonable negative values and is the one used in this study. Basically, the MART algorithm is iterated cyclically:

$$x_j^{k+1} = x_j^k \cdot \left(\frac{y_i}{\langle a_i, x^k \rangle} \right)^{\lambda_k a_{ij}} \tag{15}$$

where yi is the ith observed STEC in a column of m measurements, xj is the jth resulted cell electron density in a column of n unknowns, aij is the length of link i that lies in cell j, λ_k is the relaxation parameter at the kth iteration with $0 < \lambda_k < 1$, and the inner product of the vectors x and ai is the simulated STEC for the ith path. The electron density matrix x is therefore corrected iteratively by the ratio of the measured STEC and the simulated STEC with a relaxation parameter of λ_k until the residual does not change (see Figure 10). This relaxation parameter value is chosen from experience in which the best λ_k value is identified where the solution converges quickly with a reasonable number of iterations and the residuals are a minimum. Here λ_k =0. 01 has been chosen for all iterations. In addition, it is noted that any iterative algorithm requires an initial condition before the iteration begins. Due to the poor STEC geometry, the initialization could be extremely important for the tomographic reconstruction. In practice, the closer the initial condition is to the true electron density distribution, the more accurate the reconstruction will be. Here the latest IRI-2007 model (http://nssdcftp.gsfc.nasa.gov/models/ionospheric/iri/iri2007) is used as an initial guess for the reconstruction iteration.
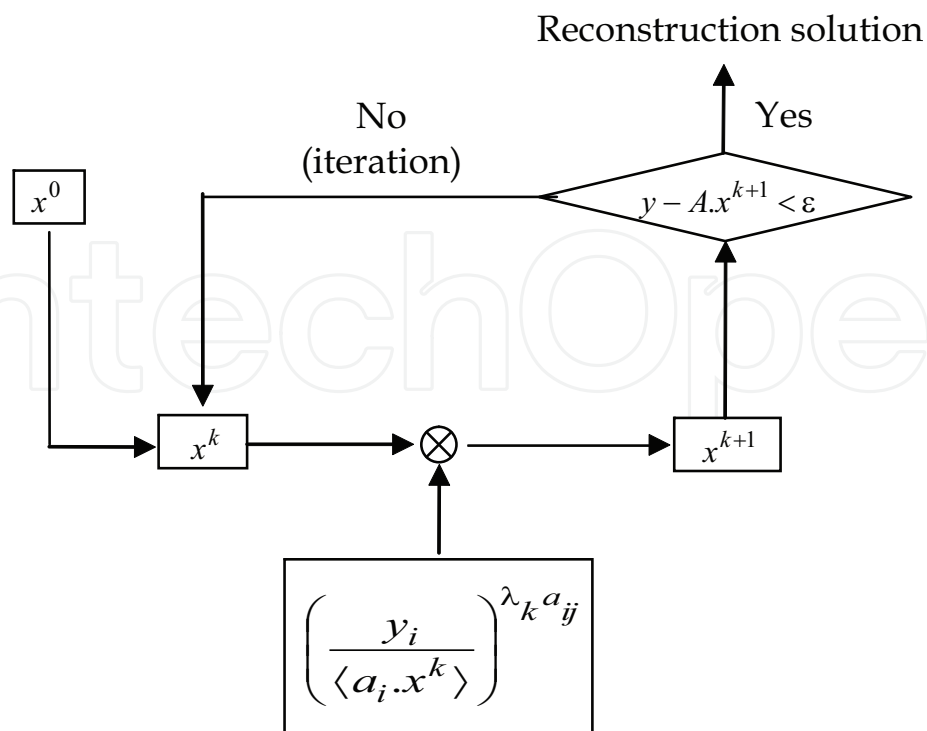

Fig. 10. Flow chart of MART

The ionospheric reconstruction algorithm MART can integrate the STEC from all available GPS receivers to all GPS satellites visible from each site of the KGN network above a user-specified elevation cut-off angle (usually 15°). The unknown electron density profile is expressed in 4-D (longitude-latitude-height and time) voxel basis functions over the following grid: longitude 124E°-130E° in 1° increments, latitude 33N°-39N° in 0.5° increments, altitude 100 km - 1000 km in 25 km increments and time: 1 h increments of linear change in the electron density per voxel. As there are a sparse number of ions in the ionosphere above 1000 km, the effect on the inversion for ionospheric electron density profiles is very small and the ionosphere is only considered up to an altitude of 1000 km. Furthermore, it is faster to invert the unknown ionospheric density parameters because of the reduced number of unknown variables. In addition, the fewer leaving rays from the ionospheric space of above defined latitude and longitude range are not used, but are useful to further obtain ionospheric profiles outside the latitudinal/longitudinal boundaries space. Using the STEC of all ray paths passing the ionospheric grid cells from the Korean GPS network, the 4-D ionospheric electron density profiles can be derived through the tomography reconstruction algorithm. To verify the reliability of GPS ionospheric tomography reconstruction results, the available ionosonde station (Anyang) in South Korea provides an independent comparison with the GPS tomographically reconstructed electron density profiles. The electron density profiles at 25 km height steps from GPS reconstruction and ionosonde data match well in October and November with a root-mean-square (RMS) of $0.3 \times 10^{11} el/m^3$. For example, Figure 11 shows a comparison of the GPS reconstructed electron density profile at 9:00 UT on 1 October 2003 with the available ionosonde data at Anyang station (37.39°N, 126.95°E) and the profiles from the IRI-2007 model. It can be seen that the GPS tomographically reconstructed density profile is in a good agreement with ionosonde data and the IRI-2007 model, but is closer to the ionosonde, which confirms the validity of our GPS ionospheric reconstruction approach (Jin et al., 2006 and 2008).

3.3 F-2 layer ionospheric response to storm

It is well known that geomagnetic storms may profoundly affect the global ionosphere and upper atmosphere, inducing great variations in such parameters as the Total Electron Content (TEC), the F2-layer peak density (NmF2) and its height (hmF2). These influences vary with location, season, local time and solar activity. The responses of the ionosphere to geomagnetic storms have been studied for several decades using moderately priced to expensive instrumentation, such as ionosondes and Incoherent Scatter Radar (ISR) (Lei et al. 2004). However, it is well known that ionospheric storms have a global impact on ionization, and under very disturbed conditions the ionospheric response to severe storms often presents significant changes in the distribution of ionization with latitude and altitude. Furthermore, ionosondes cannot measure the topside ionosphere and sometimes suffer from absorption during storms, whereas Incoherent Scatter Radars have geographical limitations. Nowadays the GPS satellites, being in high altitude orbits (~20,200 km), are very useful for studying the structure of the entire ionosphere, even the plasmasphere. Moreover, GPS is a low-cost, all-weather, near real time, and high-resolution atmospheric sounding technique. Therefore, GPS has been widely used to monitor the ionosphere (e.g. Jin et al. 2004-2007; Yin et al., 2004).
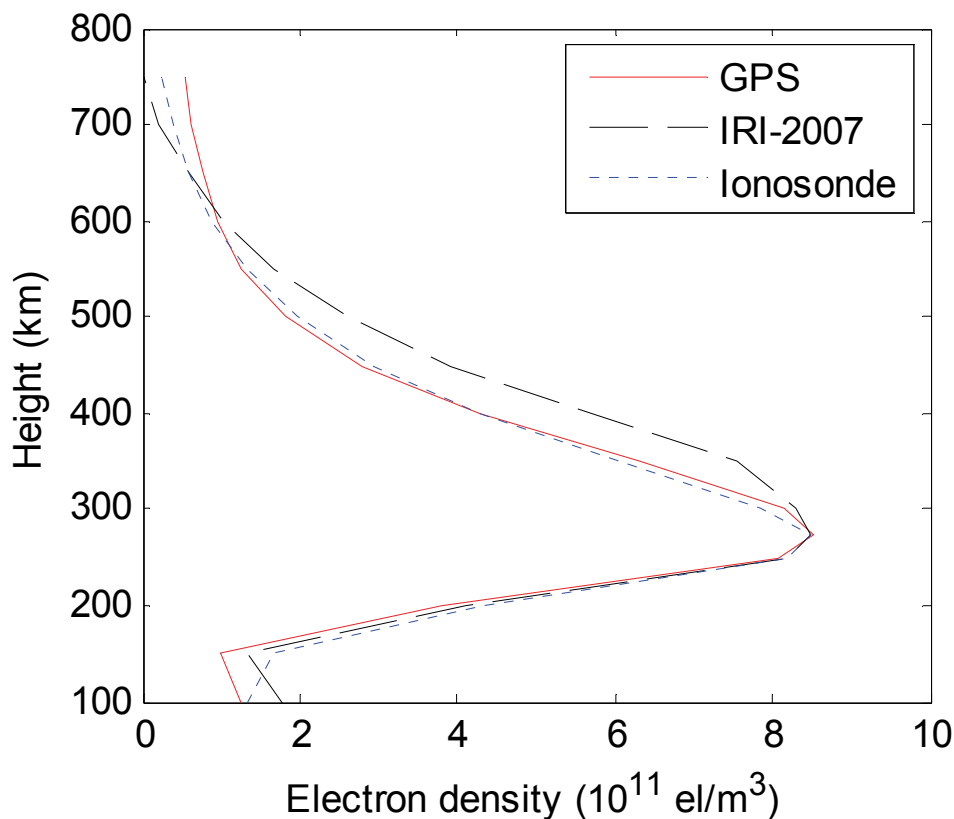
Fig. 11. Comparison of the electron density profiles derived from the ground-based GPS tomography reconstruction (solid line), ionosonde observation at Anyang stations (37.39ºN, 126.95ºE) (dot line) and IRI-2007 estimation (dashed line) at 9:00 UT on 1 October 2003

As the F2-layer peak electron density value (denoted as NmF2, proportional to the square of the F2 layer critical frequency foF2) is of great influence on the shape of the ionospheric electron density profile Ne(h), and also probably related to various physical processes of ionospheric activities as well as the F2-layer peak height (hmF2), the NmF2 and hmF2 are essential parameters for monitoring ionospheric activities and understanding the nature of the ionosphere. Although many studies of geomagnetic storms have been carried out in the US and Europe (e.g. Foster et al. 2004; Yin et al. 2004; Goncharenko et al. 2007), investigations on ionospheric behaviour to storms in Asia are relatively few due to a lack of dense sets of GPS observations, etc. In this paper, the responses of the GPS-derived NmF2 and hmF2 to the super geomagnetic storm (20 November 2003) over South Korea using data from the dense Korean GPS Network are described. First, ground-based dual-frequency GPS observations are used to produce electron density profiles using the ionospheric tomography technique, which are verified by independent ionosonde data. Then the responses of the key ionospheric F2-layer parameters NmF2 and hmF2 to the 20 November 2003 geomagnetic storm are investigated over South Korea to gain insights into the effects of different physical conditions and processes.

In the following, the 3-D ionospheric disturbances during the large November 20th 2003 geomagnetic storm are investigated and analyzed using GPS data in South Korea. The geomagnetic storm Dst, Kp and AE indices on 20-21 November 2003 obtained from the World Data Center in Kyoto (http://swdcdb.kugi.kyoto-u.ac.jp/) showed a strong geomagnetic storm on November 20th, 2003 (Figure 2).
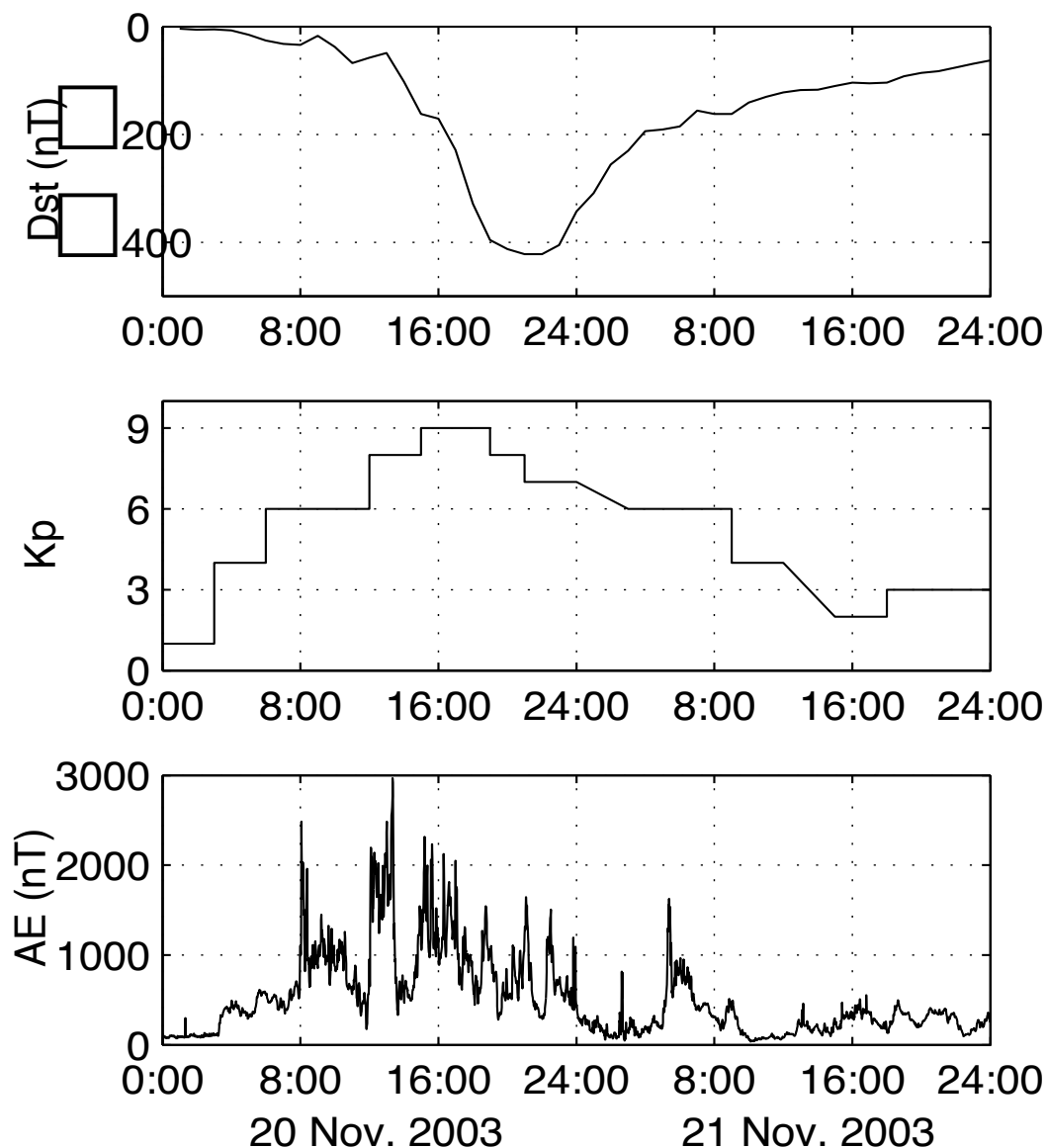
Fig. 12. The geomagnetic storm index (Dst) (upper), Kp (middle) and AE indices (bottom) on 20-21 November 2003

As the F2-layer peak electron density (NmF2) and its height (hmF2) are main parameters of the ionospheric electron density profile Ne (h), the behaviour of the ionospheric F2-layer to the storm was investigated over South Korea in terms of the NmF2 and hmF2. Here the peak density (NmF2) and its corresponding height (hmF2) are obtained from the ground-based GPS observations using the MART reconstructed tomography technique. The monthly median value of GPS reconstructed electron density profiles during the quiet days is regarded as the reference and the deviation of ionospheric NmF2 and hmF2 can reflect the ionospheric behaviors during the geomagnetic storm. It has shown that the GPS-derived NmF2 has a disturbance at 9:00 UT and then increases from 10:00 UT until 19:00 UT. The corresponding hmF2 also suddenly rises from 8:00 UT when the storm just started, and reaches the maximum height at about 16:00 UT with a maximum Kp value of 9, and then gradually descends until 21:00 UT (Fig.13), which are also supported by anther independent ionosonde measurement at Anyang station.
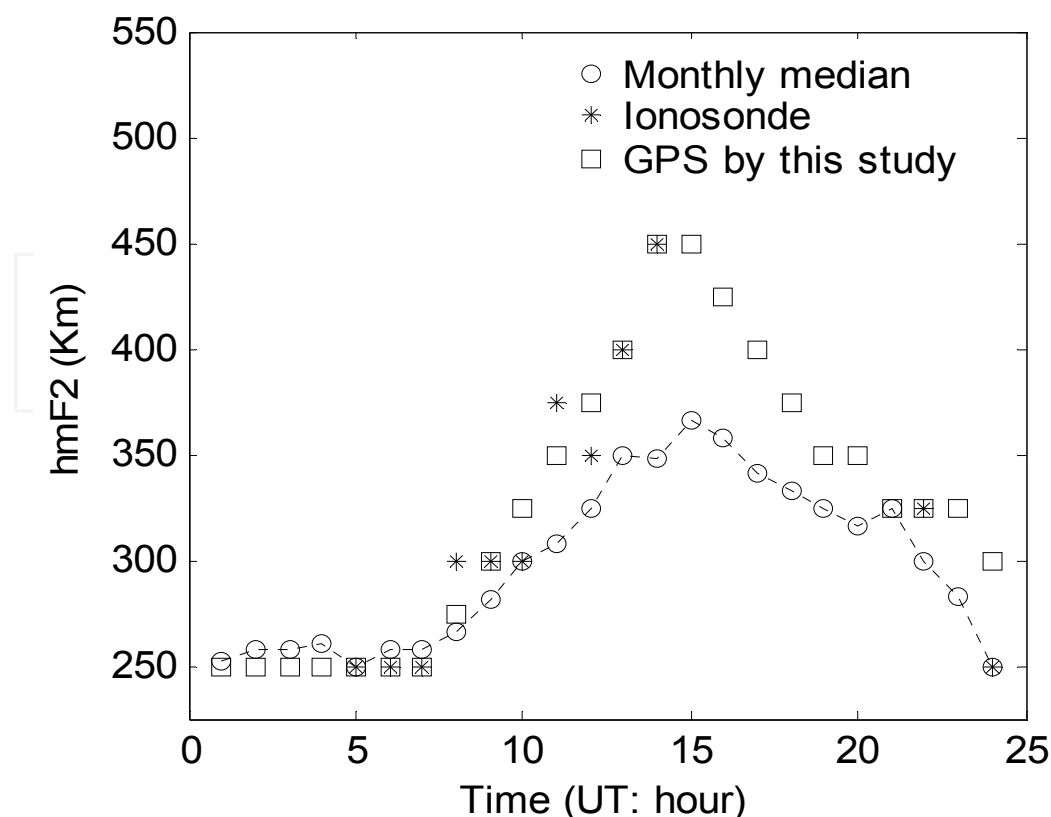
Fig. 13. The hmF2 variations from monthly median, ionosonde and GPS observations on 20 November 2003

Normally the increase/loss rate of F region electron density depends mainly on the molecular nitrogen concentration [N2] and atomic oxygen concentration [O] [8]. However, the O/N2 ratio obtained by the GUVI instrument on board the TIMED satellite doesn't show significant changes in South Korea where the increased NmF2 was observed, indicating that the increased NmF2 in South Korea is not caused by changes in neutral composition, and other possible non-chemical effects, such as dynamical changes of vertical ion motions induced by winds and E×B drifts, tides and waves in the mesosphere/lower thermosphere (MLT) region, which can be dynamically coupled upward to generate ionospheric perturbations and oscillations.

4. Conclusion

The GPS signals are delayed due to the effects of dry gas and water vapor when propagating through the neutral atmosphere. The hydrostatic delay is proportional to the surface pressure and the wet delay is a key parameter in atmospheric radiation, hydrological cycle, energy transfer and the formation of clouds via latent heat. Thereby, the total tropospheric delay (ZTD) is an important parameter of the atmosphere, which directly or indirectly reflects the weather and climate processes, variations, and atmospheric vertical motions, etc. Comparing the time series of the zenith tropospheric delay (ZTD), zenith hydrostatic delay (ZHD), zenith wet delay (ZWD), surface temperature, pressure and relative humidity, it has been noted that the ZHD is highly proportional to the atmospheric pressure at the site and relatively stable and the ZWD is positively correlated with the

temperature and correlated with the relative humidity. The mean correlation coefficient between ZWD and surface temperature is about 0.80 and the correlation coefficient between ZTD and ZWD is about 0.95, reflecting a good agreement between ZTD and ZWD variations. Therefore, the seasonal cycles of the ZTD are due primarily to the wet component (ZWD), especially in the surface temperature, even though the wet delay is only 10% of the total delay (ZTD).

The lower mean ZTD values are located at the areas of higher altitude (e.g. Tibet, Asia and Andes Mountain, South America) and higher latitude areas (Antarctica and Arctic), and the higher mean ZTD values are concentrated at the areas of middle-low latitudes. The mean ZTD decreases with increasing altitude at an exponentially decreasing rate due to the atmospheric pressure decreasing with the height increasing. The mean secular ZTD variation trend is about 1.5±0.001 mm/yr at all GPS sites. The secular variations are systematically increasing in most parts of the Northern Hemisphere and decreasing in most parts of the Southern Hemisphere (excluding increasing in Antarctic). The ZTD trends are almost symmetrically decreasing with increasing altitude, while the sum of trends at globally distributed GPS sites is almost zero, possibly reflecting that the secular ZTD variation is in balance at a global scale. The annual variation of ZTD ranges from 25 to 75 mm depending on the site, and the mean amplitude is about 50 mm at most sites. The annual variation amplitudes of ZTD at the IGS sites near Oceanic coasts are generally larger than in the continental inland. Larger amplitudes of annual ZTD variation are mostly found at middle-low latitudes (near 20S° and 40N°), and the smaller amplitudes of annual ZTD variation are located at higher latitudes (e.g. Antarctic and Arctic) and the equator areas. The phase of annual ZTD variation is almost about 60° (about February, summer) in the Southern Hemisphere and at about 240° (about August, summer) in the Northern Hemisphere. The mean amplitude of semiannual ZTD variations is about 10 mm, much smaller than annual variations. The significant semiannual variations with a consistent phase of about 30° (about January) are at above 30°N in the Northern Hemisphere and the amplitudes of semiannual variations in other parts are not significant. In addition, the higher frequency variability (RMS of the ZTD residuals) ranges from 22 to 40 mm of delay, once again primarily due to the wet component. The variability depends on altitude of the station. Inland stations tend to have lower variability and stations at ocean and coasts have higher variability. This is because these stations in particular are located in a region well known for large abrupt changes in the weather, such as Indian, West Pacific and West Atlantic oceans.

In addition, the responses of the key ionospheric F2-layer parameters (NmF2 and hmF2) to the 20 November 2003 super storm have been studied using the GPS ionospheric tomography technique over South Korea. A strong increase of NmF2 during this storm has been found, accompanied by a significant hmF2 uplift, which is also confirmed by independent ionosonde observations. The uplift of the F2 layer is mainly associated with a strong eastward electric field. The increase of electron density in the F2-layer peak depends mainly on the molecular nitrogen concentration [N2] with some contribution from molecular oxygen concentration [O2], while the production rate depends on the atomic oxygen concentration [O]. However, the O/N2 ratio from the GUVI instrument on board the TIMED satellite shows no significant change during this geomagnetic storm. It suggests that the increase in NmF2 is not caused by changes in neutral composition, but is related to other

possible non-chemical effects, such as dynamical changes of vertical ion motions induced by winds and E×B drifts, tides and waves in the mesosphere/lower thermosphere (MLT) region, which can be dynamically coupled upward to generate ionospheric perturbations and oscillations.

Ground-based and space borne GPS observations have been widely used in atmospheric sounding, including sensing tropopsheric precipitable water vapor (PWV), ionospheric total electron content (TEC) and atmospheric profile information (e.g., pressure, temperature, humidity, tropopause and ionospheric electron density). These observations have facilitated greater advancements in meteorology, climatology, numerical weather model, atmospheric science and space weather (e.g., Jin et al., 2007; Jin et al., 2009; Schmidt, et al. 2010). For example, the dual frequency ground GPS array could detect ionospheric response and its processes during large geomagnetic storms (Jin et al., 2008). Meanwhile, ground GPS also observed the plasma bubbles and retrieved reliable propagation characteristics of the depletions without assumptions about the mapping of the depletion along magnetic field lines to large latitudinal distances, comparable with airglow data (Haase et al., 2011).

Additionally, space-borne GPS receivers have proven very successful in making high vertical resolution and global atmospheric measurements using the radio occultation (RO) technique The existing GPS radio occultation (RO) missions have been widely used to estimate the detailed vertical profile information, including pressure, temperature, gravity waves and sporadic E-layers as well as their variation characteristics, particularly six satellites of the Taiwan/US FORMOSAT-3/COSMIC (FORMOsa SATellite mission-3/Constellation Observing System for Meteorology, Ionosphere and Climate) mission with more than 2000 radio occultation profiles per day. Schmidt et al. (2010) was the first to observe upper tropospheric warming and lower stratospheric cooling using GPS RO data (2001-2009). Although a number of progresses in atmospheric and ionospheric sensing have been made using GPS RO missions in the past few years, they still do not satisfy actual requirements for short-time scales and higher temporal-spatial resolution monitoring together with ground GNS observations. For instance, the tropospheric or ionospheric profile information cannot be directly estimated from GPS tomography due to the lack of enough line-of-sight GPS signals passing each grid cell (Jin et al., 2006 and 2008; Nesterov and Kunitsyn, 2011). Moreover, most current RO satellite missions are approaching their end of operations. With the increase of future GNSS satellite constellations and more GNSS RO missions, the goal of improved temporal-spatial resolution will enable more detailed profile information and evolution processes of the atmosphere and ionosphere.

5. Acknowledgement

6. References

Austen, J. R.; S. J. Franke, and C. H. Liu, Application of computerized tomography techniques to ionospheric research, in Radio Beacon contributions to the study of ionization and dynamics of the ionosphere and to corrections to geodesy and

technical workshop, A. Tauriainen, Eds. pp. 25-35, Ouluensis Universitas, Oulu, Finland, 1986.

Beutler G., M. Rothacher, S. Schaer, T.A. Springer, J. Kouba, R.E. Neilan (1999), The International GPS Service (IGS): An Interdisciplinary Service in Support of Earth Sciences, Adv. Space Res. 23(4) 631-635, 1999.

Bevis M., S. Businger, S. Chiswell, et al. (1994), GPS Meteorology: Mapping Zenith Wet Delays Onto Precipitable Water, J. App. Meteor., 33, 379-386.

Byun, S.H., Y. Bar-Sever, and G.Gendt (2005), The new tropospheric product of the International GNSS service, paper presentaed at 2005 ION GNSS conference, Inst. of Navig., Long Beach, Calif.

Dai A, Wang J (1999) Diurnal and Semidiurnal Tides in Global Surface Pressure Fields. J Atmos Sci 56, 3874-3891.

Dai A, Wang J, Ware RH, Van Hove T (2002) Diurnal variation in water vapor over North America and its implications for sampling errors in radiosonde humidity. J Geophys Res 107(D10): 4090, doi:10.1029/ 2001JD000642.

Davis, J.L., T.A. Herring, I. Shapiro, A. Rogers, and G.Elgered (1985), Geodesy by radio interferometryL Effects of atmospheric modeling errors on esimatetes of baseline length, Radio Sci., 20(6), 1593-1607.

Deblonde G., S. Macpherson, Y. Mireault , et al.(2005), Evaluation of GPS precipitable water over Canada and the IGS network, Journal of Applied Meteorology, 44 (1): 153-166.

Elgered, G., et al. (1997), Measuring Regional Atmospheric Water Vapor Using the Swedish Permanent GPS Network, Geophysical Research Letters, 24, 2663-2666.

Feng, D., Herman B.M. Remotely sensing the earth's atmosphere using the Global Positioning System (GPS)- The GPS/MET data analysis. Journal of Atmospheric and Oceanic Technology, 16, 989-1002, 1999.

Foster J, Coster A, Erickson P, Rich F, Sandel B (2004) Stormtime observations of the flux of plasmaspheric ions to the dayside cusp/magnetopause, Geophys Res Lett 31: doi:10.1029/2004GL020082.

Goncharenko LP, Foster J, Coster A, Huang C, Aponte N, Paxton L(2007) Observations of a positive storm phase on September 10, 2005, J Atmos Solar Terr Phys 69: 1253-1272.

Gordon R, Bender R, Therman G (1970) Algebraic Reconstruction Techniques (ART) for three Dimensional Electron Micoscopy and X-ray Photography. J Theor.Biol 29: 471-481

Haase, J., M. Ge, H.Vedel and E. Calais (2003),Accuracy and Variability of GPS Tropospheric Delay Measurements of Water Vapor in the Western Mediterranean, Journal of Applied Meteorology,42(11): 1547-1568.

Hagemann S., L. Bengtsson and G. Gendt (2003), On the determination of atmospheric water vapor from GPS measurements, J. Geophys. Res., 108 (D21): 4678, doi:10.1029/2002JD003235.

Hajj, G.A., Romans, L.L. Ionospheric Electron Density Profiles Obtained with the Global Positioning System: Results from the GPS/MET Experiment. Radio Science, 33(1): 175-190, 1998.

Haase, J.S., T. Dautermann,, M.J. Taylor, N. Chapagain, E. Calais,, D. Pautet, Propagation of plasma bubbles observed in Brazil from GPS and airglow data. Adv. Space Res. doi: 10.1016/j.asr.2010.09.025, 2011.

Jin SG, Wang JL, Zhang HP, Zhu WY (2004), Real-time monitoring and prediction of the total ionospheric electron content (TEC) by means of GPS. Chinese Astronomy and Astrophysics 28(3): 331-337.

Jin S.G., and P.H. Park (2005), A new precision improvement of zenith tropospheric delay estimates by GPS, Current Science, 89 (6): 997-1000.

Jin SG, Park J, Wang J, Choi B, (2006), Electron density profiles derived from ground-based GPS observations. Journal of navigation 59(3): 395-401.

Jin SG, Park J, Cho J, Park P (2007), Seasonal variability of GPS-derived Zenith Tropospheric Delay (1994-2006) and climate implications. J Geophys Res 112: D09110, doi: 10.1029/2006JD007772.

Jin, S.G., O. Luo, and P. Park (2008), GPS observations of the ionospheric F2-layer behavior during the 20th November 2003 geomagnetic storm over South Korea, J. Geod., 82(12), 883-892, doi: 10.1007/s00190-008-0217-x.

Jin, S.G., O. Luo, and S. Gleason (2009), Characterization of diurnal cycles in ZTD from a decade of global GPS observations, J. Geod., 83(6), 537-545, doi: 10.1007/s00190-008-0264-3.

King R.W. and Y. Bock (1999), Documentation for the GAMIT GPS Analysis Software, Mass. Inst. of Technol., Cambridge Mass.

Lei J, Liu L, Wan W, Zhang S (2004) Modeling the behavior of ionosphere above Millstone Hill during the September 21-27, 1998 storm. Journal of Atmospheric and Solar-Terrestrial Physics 66: 1093-1102.

Manuel H., J. Juan, J. Sanz, et al. (2001), A New Strategy for Real-Time Integrated Water Vapor Determination in WADGOPS Networks, Geophy. Res. Lett., 28(17), 3267-3270.

Nesterov, I.A., V.E., Kunitsyn, GNSS radio tomography of the ionosphere: The problem with essentially incomplete data, Advances in Space Research, doi: 10.1016/j.asr.2010.11.034, 2011.

Niell A.E. (1996), Global Mapping Functions for the Atmospheric Delay at Radio Wavelengths, Journal of Geophysical Research, 101(B2), 3227-3246.

Raymund TD, Austen JR, Franke SJ (1990) Application of computerized tomography to the investigation of ionospheric structures. Radio Science 25: 771-789.

Rocken, C. Analysis and validation of GPS/MET data in the neutral atmosphere. Journal of Geophysical. Research, 102: 29849-29866, 1997.

Saastamoinent J. (1973), Contribution to the theory of atmospheric refraction, Bulletin Geodesique, 107, 13-34.

Schmidt, T., Wickert, J., and Haser, A. (2010), Variability of the upper troposphere and lower stratosphere observed with GPS radio occultation bending angles and temperatures, Adv. Space Res., 46(2),150-161,doi:10.1016/j.asr.2010.01.021

Syndergaard, S. On the Ionosphere Calibration in GPS Radio Occultation Measurements. Radio Science, 35(3): 865-883, 2000.

Tsai LC, Liu CH, Tsai WH, Liu CT (2002) Tomographic imaging of the ionosphere using the GPS/MET and NNSS data. J. Atmos. Sol. Terr. Phys. 64, 2003-2011.

Tregoning P., R. Boers and D. O'Brien (1998) Accuracy of Absolute Precipitable Water Vapor Estimates from GPS Observations, Journal of Geophysical Research, 103(28), 701-710.

Wagner, C.. Kloko, J. The value of ocean reflections of GPS signals to enhance satellite altimetry: data distribution and error analysis. Journal of Geodesy, 74, 128-138, 2003.

Westwater, E. R. (1993), Ground-based microwave remote sensing of meteorological variables. Atmospheric Remote Sensing by Microwave Radiometry, M. A. Janssen, Ed., J. Wiley and Sons, Inc., 145-213.

Yin P, Mitchell CN, Spencer PS, Foster JC (2004) Ionospheric electron concentration imaging using GPS over the USA during the storm of July 2000. Geophys Res Lett 31: L12806, doi: 10.1029/2004GL019899.

Global Navigation Satellite Systems: Signal, Theory and Applications

Edited by Prof. Shuanggen Jin

Global Navigation Satellite System (GNSS) plays a key role in high precision navigation, positioning, timing, and scientific questions related to precise positioning. This is a highly precise, continuous, all-weather, and real-time technique. The book is devoted to presenting recent results and developments in GNSS theory, system, signal, receiver, method, and errors sources, such as multipath effects and atmospheric delays. Furthermore, varied GNSS applications are demonstrated and evaluated in hybrid positioning, multi-sensor integration, height system, Network Real Time Kinematic (NRTK), wheeled robots, and status and engineering surveying. This book provides a good reference for GNSS designers, engineers, and scientists, as well as the user market.

How to reference

In order to correctly reference this scholarly work, feel free to copy and paste the following:

Shuanggen Jin (2012). GNSS Atmospheric and Ionospheric Sounding – Methods and Results, Global Navigation Satellite Systems: Signal, Theory and Applications, Prof. Shuanggen Jin (Ed.), ISBN: 978-953-307-843-4, InTech, Available from: http://www.intechopen.com/books/global-navigation-satellite-systems-signal-theory-and-applications/gnss-atmospheric-and-ionospheric-sounding-methods-and-results

INTECH
open science | open minds